MATERIALS SCIENCE

# Wax-wetting sponges for oil droplets recovery from frigid waters

P. Cherukupally[1,2]*, W. Sun[3†], D. R. Williams[2], G. A. Ozin[3]*, A. M. Bilton[1]*



**Energy-efficient recovery of oil droplets from ice-cold water, such as oil sands tailings, marine, and arctic oil spills, is challenging. In particular, due to paraffin wax crystallization at low temperatures, the crude oil exhibits high viscosity, making it difficult to collect using simple solutions like sponges. Here, we report a wax-wetting sponge designed by conforming to the thermoresponsive microstructure of crude oil droplets. To address paraffin wax crystallization, we designed the sponge by coating a polyester polyurethane substrate with nanosilicon functionalized with paraffin-like octadecyl ligands. The wax-wetting sponge can adsorb oil droplets from wastewater between 5° and 40°C with 90 to 99% removal efficacy for 10 cycles. Also, upon rinsing with heptol, the adsorbed oil is released within seconds. The proposed approach of sponges designed to conform with the temperature-dependent microstructure of the crude oils could enable cold water technologies and improve circular economy metrics in the oil industry.**

## INTRODUCTION

Recovering multiphase oil droplets from ice-cold effluents, seen in the over 1 trillion liters of oil sands tailings, marine, and arctic oil spills, is challenging. At low temperatures, because of thermoresponsive phase change in crude oil, its surface chemistry varies, and viscosity increases, making oil droplets recovery difficult (*1*–*3*). Traditional technologies, such as hydrocyclones, floatation devices, and inclined plate separators, are either energy intensive or ineffective for separating oil droplets smaller than 20 μm (*4*). Recently, surface-engineered sponges (SEnS) have emerged as low-cost solutions for reclaiming oil field effluents (*5*–*7*). To overcome the viscosity challenge, photothermal sponges were applied to remove oil from the marine surface by melting viscous crude oil at 90°C (*8*, *9*). Although this approach collects oil quickly, in situ heating is energy intensive for recovering dilute emulsions, especially at concentrations ≤10,000 ppm, typically seen in these effluents. Moreover, at elevated temperatures, the volatile organics from the crude oil either dissolve or evaporate, amplifying their toxicological effect. Alternatively, SEnS designed with critical surface energy have shown excellent performance in recovering crude oil droplets from wastewater (*5*, *10*, *11*). However, the influence of low temperatures on multiphase emulsions formation and their removal in relation to sorbent design are not completely understood. Furthermore, the kinetic performance of SEnS for dilute, multiphase emulsion recovery from cold water is yet to be assessed. By understanding the causality for the multiphase behavior of oil droplets that occurs at low temperatures, we could design sponges with conforming surface properties for droplets recovery using energy-efficient, sustainable strategies.

In this work, we hypothesize that conforming the surface wetting properties of sponges to the thermoresponsive morphology of oil droplets could result in their effective adsorption of droplets from cold water, despite their multiphase behavior and higher viscosity. Crude oil is a diverse mixture of saturates, aromatics, resins, and asphaltenes. At low temperatures, the saturated wax crystallizes to the oil surface (Fig. 1A). These crystallites increase the viscosity of crude oil (*12*), causing droplets to coalesce, and become multiphase emulsions (Fig. 1B) (*13*, *14*). Therefore, a sponge with conforming wax-wetting properties could adsorb multiphase oil droplets from cold effluents by attaching to sticky wax crystallites at the droplets' surface (Fig. 1C). Subsequently, the adsorbed crude oil can be collected by displacing it with miscible, green solvents, enabling regenerated sponge reuse and crude oil recycling.

In this work, we report a wax-wetting sponge engineered with paraffin-like surface groups (SEnS-P) for recovering multiphase oil droplets from cold effluents. The selected crude oil contains paraffin waxes, which are linear, long-chain hydrocarbons. Therefore, SEnS-P was fabricated by coating a polyester polyurethane (PESPU) sponge with nanosilicon capped with paraffin-like, octadecyl ligands (ncSi-$C_{18}$). Because of enhanced wax-wetting properties, SEnS-P adsorbed oil droplets between 5° and 40°C with 90 to 99% removal efficacy within 180 min. The adsorbed crude oil was recovered within a few seconds by rinsing with a mixture of heptane and toluene (heptol). The regenerated SEnS-P also adsorbed oil droplets with 90 to 99% removal efficacy for 10 cycles. This approach of designing sponges that conform to the thermoresponsive morphology of droplets could revolutionize the design of energy-efficient sorbents for oily wastewater reclamation. This methodology could be extended to design materials for separating other viscous organic pollutants from industrial effluents, such as petrochemicals, lubricants, and paints.

## RESULTS

### Chemical structure of the crude oil

To design a wax-wetting sponge, we need to know the chemical structure of the crude oil, especially thermoresponsive waxes. According to the solubility class, the major constituents of the crude oil are saturates (62.95%), aromatics (37.05%), resins (8.7%), and asphaltenes (1.19%) (*11*). The selected crude oil also contains approximately 2.44% of natural paraffin wax (a subclass of saturates). The paraffin wax is a group of *n*-alkanes with a few or no branches. The waxes crystallize into liquid and solid crystals below cloud point temperature ($T_{cloud}$) and pour point temperature ($T_{pour}$), respectively.

[1]Department of Mechanical and Industrial Engineering, University of Toronto, Toronto, Canada. [2]Department of Chemical Engineering, Imperial College London, London, UK. [3]Department of Chemistry, University of Toronto, Toronto, Canada.
*Corresponding author. Email: p.cherukupally17@imperial.ac.uk (P.C.); g.ozin@utoronto.ca (G.A.O.); bilton@mie.utoronto.ca (A.M.B.)
†Present address: State Key Laboratory of Silicon Materials and School of Material Science and Engineering, Zhejiang University, Hangzhou, China.

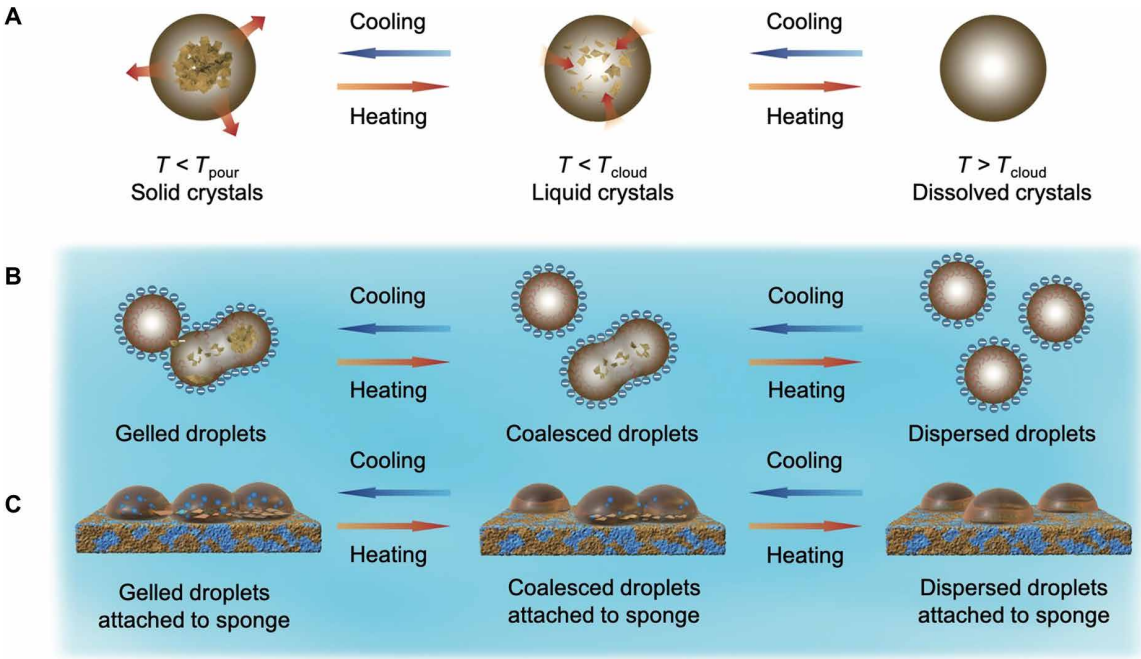


**Fig. 1. Thermoresponsive behavior of crude oil droplets and their removal using a wax-wetting sponge.** Left to right: (**A**) With cooling, wax transitions from dissolved to liquid crystalline phase below cloud point temperature ($T_{cloud}$) and solid crystalline phase below pour point temperature ($T_{pour}$). (**B**) At low temperatures, because of jamming of wax crystallites and Ostwald ripening, the oil droplets partially coalesce and become multiphase droplets and gels. (**C**) A wax-wetting sponge could adsorb the multiphase oil droplets from water by attaching liquid and solid wax crystallites present at droplets' surface.

The detailed chemical structures of the aliphatic and aromatic groups at the crude oil surfaces were determined using mass spectroscopy (see table S1). The major ion peaks in the spectra are presented as the $C_xH_y^+$ fragments, where $x \approx \frac{1}{2}y$ represents aliphatic structures and $x \approx y$ represents aromatic structures. For simplicity, the discussion is limited to relevant aliphatic-aromatic structures, but not other heteroatoms, such as N, O, and S. In the positive-ion spectrum (Fig. 2A), the ion signals at mass/charge ratio ($m/z$) 43 ($C_3H_7^+$), 57 ($C_4H_9^+$), 71 ($C_5H_{13}^+$), and 221 ($C_{16}H_{29}^+$) and most of the signals correspond to aliphatic groups. The minor ion signals at $m/z$ 91 ($C_7H_7^+$), 117 ($C_9H_9^+$), and 189 ($C_{15}H_{19}^+$) correspond to fragments containing aromatic groups. In high–molecular weight spectra (Fig. 2B), the peaks at $m/z$ 265 ($C_{19}H_{37}^+$), 281 ($C_{21}H_{30}^+$), 326 ($C_{24}H_{38}^+$), and 341 ($C_{25}H_{41}^+$) suggest the presence of a small number of organics in the range of $C_{19}$ to $C_{25}$. The phase separation of chemical groups at the crude oil surfaces with temperature was observed in the spatial spectra at $m/z$ 0 to 250 (fig. S1, A and B). At 10°C, the crude oil surface is densely covered with aliphatic groups that appear as large plates (bright yellow). However, with the increase in temperature from 10° to 27°C, the aliphatic groups have melted into smaller plates. The plate shape of the chemical groups resembles that of paraffin wax groups. The mass spectroscopy results suggest that a conforming wax-wetting sponge would require surface groups with an approximate carbon chain length between $C_3$ and $C_{25}$.

## Wax phase change with temperature

The adsorption of oil droplets onto solid surfaces relies on the phase behavior, rheology, and adhesion properties of the crude oil with temperature (*15*). In thermogram of crude oil (Fig. 2C), the endothermic (down) peak represents the wax phase change behavior upon heating. The polarized microscope images (insets) show the corresponding phases of the wax. The first inset shows a lump of solidified wax crystallites at the crude oil surface below 12°C. The endothermic peak at 12°C ($T_{pour}$) suggests that the crystallites underwent a sharp phase transition from solid to liquid due to heating (*15*). The endothermic onset at 38°C ($T_{cloud}$) suggests that liquid crystals of wax began to dissolve. The corresponding inset between 38° and 12°C shows that the crystallites melted from a solid lump into fragments of liquid crystals. Above 38°C, the linear curve and the plane oil surface shown in the inset indicate that the wax crystals have completely dissolved into the crude oil. On the basis of the thermal analysis, three temperatures, 5°, 20°, and 40°C, corresponding to the solid, liquid, and dissolved phases, were selected for evaluating the influence of the wax phase on the sponge performance. The selected temperatures also represent commonly observed oil field wastewater temperatures.

## Rheological and adhesion properties

On the basis of the thermogram, the wax crystallizes at 38° and 12°C as liquid and solid wax crystals, respectively. These crystals offer resistance to flow, leading to a marked increase in the crude oil viscosity at these temperatures (fig. S1C). Because of precipitation of liquid wax crystallites, near $T_{cloud}$, with the decrease in temperature from 40° to 35°C, the viscosity suddenly increased from 26 to 85 mPa·s (a 218% increase). Similarly, near $T_{pour}$, with the reduction in temperature from 15° to 10°C, due to solid wax crystallites, the viscosity once again suddenly increased from 470 to 2607 mPa·s (a 454% increase). With further cooling to 5°C, the agglomerated solid crystals increase the viscosity to 36,504 mPa·s (compared to viscosity at 10°C, a 1414% increase). The influence of wax crystallites on the viscoelastic properties of the crude oil at practically relevant temperatures is investigated in detail below.

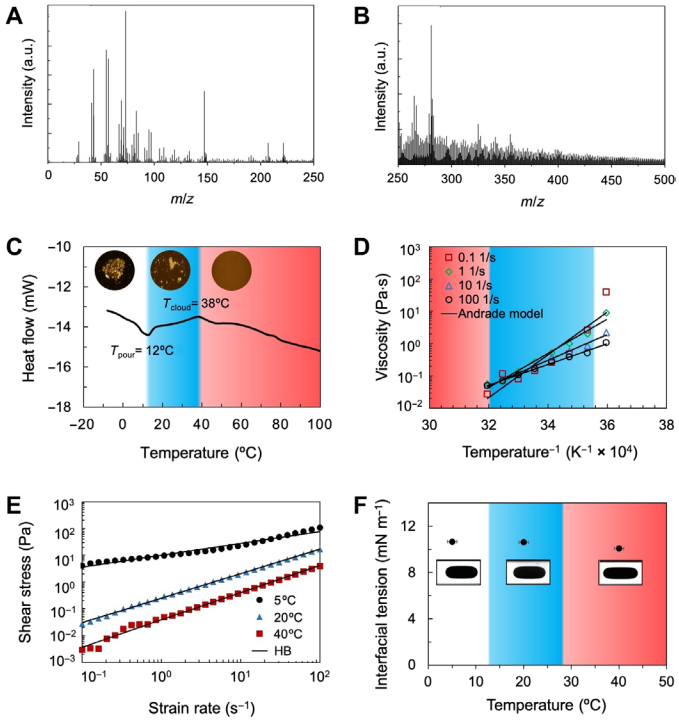


**Fig. 2. Chemical structure and rheological properties of crude oil.** Mass spectrum at (**A**) *m/z* 0 to 250 shows that the crude oil contains aromatic and aliphatic groups, and mass spectrum at (**B**) *m/z* 250 to 500 shows high-molecular organic groups in the range of $C_{16}$ to $C_{25}$. a.u., arbitrary units. Thermoresponsive behavior of crude oil: (**C**) Thermogram of crude oil shows cloud point temperature ($T_{cloud}$) and pour point temperature ($T_{pour}$). The corresponding phases of the wax are shown in the insets. (**D**) The viscosity of crude oil is described using the Andrade expression. (**E**) Flow curves are described with the Herschel-Buckley (HB) model. Because of the crystallization of waxes, the viscosity and plasticity of crude oil increased with decreasing temperature. (**F**) Oil/water interfacial tension shows a negligible variation with temperature. In (A) and (B), the bin size is 10. In (D) to (F), the data are an average of three measurements.

Figure 2D shows the viscosity of crude oil with temperature and shear rate, described with the Andrade expression (*16*, *17*)

$$\eta = A e^{b/T} \quad (1)$$

where η is the viscosity (Pa·s), $T$ is the absolute temperature (K), and $A$ and $b$ are constants. The viscosity of crude oil increased with decreasing temperature and shear rate. At higher shear rates of 100 and 10 $s^{-1}$, the Andrade expression accurately represented measured viscosity. However, the viscosity deviated from the expression at lower shear rates of 1 and 0.1 $s^{-1}$ (table S2). For high shear rates, near $T_{cloud}$ and $T_{pour}$, the increase in viscosities was 28 and 30%. Near $T_{cloud}$ and $T_{pour}$, at 1 $s^{-1}$, the viscosity slightly increased by 36 and 100%, but at 0.1 $s^{-1}$, viscosity markedly increased by 326 and 455%. This trend suggests that the wax crystallization is higher at lower shear rates. The influence of wax crystals on the crude oil flow behavior (Fig. 2E) can be understood using the Herschel-Bulkley model

$$\tau = \tau_o + k(\gamma)^n \quad (2)$$

where τ is the shear stress (Pa), $\tau_o$ is the yield stress (Pa), $k$ is the consistency factor, γ is the shear rate ($s^{-1}$), and $n$ is the flow index. The crude oil flow behavior changed from Newtonian at higher shear rates (100 and 10 $s^{-1}$) to non-Newtonian at lower shear rates (1 and 0.1 $s^{-1}$). At 40°C, the oil followed Newtonian flow behavior with no yield stress (table S3). While, at 20° and 5°C, because of the presence of wax crystallites, the yield stress began to increase, causing the oil to follow a Bingham plastic trend. Qualitatively, the observed flow behavior with temperature and shear rate is typical in paraffin crude oils (*18*, *19*). These rheological properties suggest that the crude oil's flowability is hindered by the temperature and shear rate, making the oil removal from cold effluents challenging.

The adhesion of oil droplets to solid surfaces relies on the oil-water interfacial tension ($\gamma_{ow}$). $\gamma_{ow}$ was measured with water at 5°, 20°, and 40°C using the spinning drop method, and the oil-water interfacial tension was calculated using Vonnegut equation (*20*)

$$\gamma_{ow} = \frac{(\rho_1 - \rho_2)\,\omega^2 R^3}{4} \quad (3)$$

where $\rho_1$ and $\rho_2$ are the density of water and crude oil, ω is the angular velocity, and $R$ is the droplet radius. As shown in Fig. 2F, from 5° to 40°C, $\gamma_{ow}$ decreased slightly from 10.65 to 10.05 mN $m^{-1}$ (about 6%). The corresponding insets show that, with increasing temperature, the droplets stretched, but the diameter decreased by approximately 5.66% (table S4). Because of interfacial compounds, such as asphaltenes and resins, the dynamic changes in $\gamma_{ow}$ are usually negligible (*14*, *21*). Thus, the oil droplets could thermodynamically adsorb onto the sponge designed with critical surface energy across a broad range of temperatures.

## Formation of multiphase emulsions

Figure 3A shows the temperature-dependent phase changes in the emulsified crude oil droplets. At 40°C (right), the droplets were stable in Brownian motion, probably due to interfacial asphaltenes and resins, which act like natural surfactants (*21*). The corresponding polarized image (Fig. 3B) shows no wax crystallites, and the zoomed-in fluorescence image (Fig. 3C) shows the oil droplet (green) surrounded by water (water). Upon cooling to 20°C (middle), the droplets began to agglomerate and formed larger droplets, and the small wax crystallites were visible at the oil/water interface. This partial coalescence of droplets could be due to jamming of interfacial wax crystallites and Ostwald ripening (*14*, *22*). The corresponding fluorescence image shows a small amount of water trapped inside the oil droplet, indicating the formation of a double emulsion. With further cooling to 5°C (left), the agglomeration of oil droplets, the crystallization of wax, and the entrapment of water inside the oil droplets have increased, causing the emulsions to become a viscous gel. These observations suggest that due to dissolved, liquid, and solid crystalline phases of wax, the viscosity of the droplets may increase, causing the emulsions to transform from stable droplets to double emulsions or gels. The amount of water trapped inside the oil droplets varies over temperature, which increases the complexity of the droplets and makes the design of adsorbent challenging. However, the cross-polarized images show that the wax crystallites exist across all the phases of emulsions at the surface of the droplets. Therefore, we could design a sponge favorable for wetting the wax crystallites.

## Design and fabrication of nanocoating and SEnS-P

Previously, we reported fabrication of SEnS using ncSi-$C_{10}$ nanocoating (*11*). Here, we optimized the nanocoating by conforming

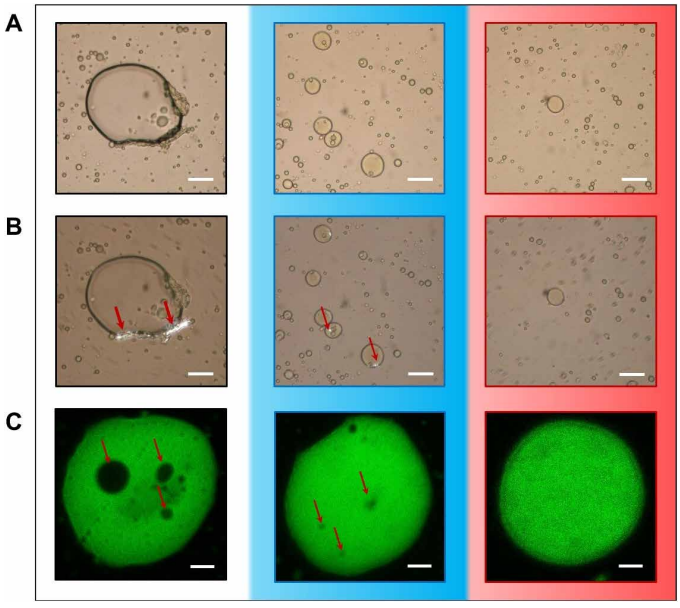


**Fig. 3. Formation of multiphase emulsions with cooling.** (**A**) Light microscope images show droplet agglomeration and coalescence with decreasing temperature. (**B**) Polarized microscope images show the crystallized wax accumulated at the surface and interface of the oil droplets. (**C**) The fluorescence images show that the amount of water (black) entrapped inside the oil (green) droplets has increased with decreasing temperature. At lower temperatures, because of wax crystallites and water entrapment, the oil droplets transformed from stable oil droplets (right) to double emulsions (middle) and a viscous gel (left). Background colors represent temperature regimes at approximately 5°C (white), 20°C (blue), and 40°C (red), where the waxes are in solid, liquid, and dissolved phases, respectively. Scale bars, 50 μm (A and B) and 2 μm (C).

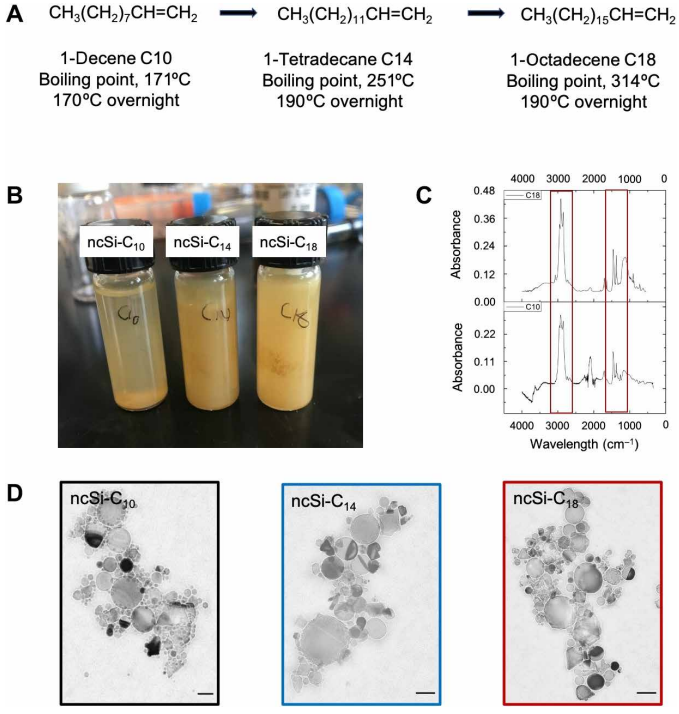


**Fig. 4. Synthesis and stability of nanocoatings.** (**A**) Synthesis of nanocoating with 1-decene, 1-tetradecene, and 1-octadecene using the thermal hydrosilylation reaction. (**B**) ncSi-$C_x$ suspended in the hexane. With increasing alkyl ligand chain length, the stability of the suspension improved. Among the three suspensions, ncSi-$C_{18}$ shows higher stability. Photo credit: W. Sun, University of Toronto. (**C**) FT-IR spectra of ncSi-$C_{10}$ versus ncSi-$C_{18}$. Because of the higher temperature, a larger number of alkyl ligands were attached to ncSi-$C_{18}$. The decrease in Si—H intensity compared to $CH_x$ intensity suggests that higher reaction temperature enhanced $CH_x$ capping, which leads to higher oleophilicity. (**D**) Transmission electron microscopy images show the nanosilicon (ncSi) capped with 10, 14, and 18 carbons, respectively. The images were background-subtracted and contrast-adjusted within the limits of the histogram. Scale bars, 100 nm.

with the thermoresponsive morphology of oil droplets. The optimized sponge, referred to as a wax-wetting sponge, was evaluated to determine compatible aliphatic-aromatic surface groups, uniform roughness, and critical surface energy. A PESPU sponge was selected as the substrate because of its favorable chemical structure. Similar to crude oil, the PESPU sponge contains aliphatic groups from ester and aromatic groups from urethane (*23*, *24*). Because of its nontoxicity, accessibility, designable surface chemistry, and future potential for degrading organics by photocatalysis (*25*), nanosilicon was chosen for tailoring the surface properties of PESPU.

A coating that conforms with crude oil microstructure was selected by comparing three nanosuspensions, ncSi covalently capped with alkyl chains of length 10, 14, and 18 carbons, namely, ncSi-$C_{10}$, ncSi-$C_{14}$, and ncSi-$C_{18}$, respectively (Fig. 4A). These nanocoatings were synthesized using thermal hydrosilylation (*26*–*28*) between Si—H on the surface of ncSi and the carbon double bond. The ncSi-$C_{18}$ solution appeared the most uniform, suggesting the best colloidal dispersibility in hexane (Fig. 4B). The Fourier transform infrared (FTIR) spectra showed that ncSi-$C_{18}$ exhibited a higher reaction extent (more intense $CH_x$ signal at ~2900 $cm^{-1}$ relative to the unreacted Si—H bond at ~2100 $cm^{-1}$), indicating a higher density of alkyl ligand attachment to ncSi (Fig. 4C). Figure 4D shows high-contrast ncSi-$C_x$ crystallites observed under the transmission electron microscope. The nanoparticles appear as large aggregates with a variable size distribution, but the thin organic layer around them is not discernible. The larger ncSi particles could be used to identify the presence of alkyl functional groups at the sponge surface upon applying the nanocoating. SEnS were fabricated by coating PESPU (film and sponges) with three nanocoatings using the established dip-and-dry coating method (*11*). The bonding between the nanocoating and the polymer was enhanced using annealing (fig. S2A). As shown in FTIR spectra (fig. S2, B to D), heating PESPU, ncSi-$C_x$, and their composite (i.e., SEnS) at 170°C have increased C═O and C—O peaks due to oxidation. Heating at high temperatures provides activation energy for oxygen-involved radicals to readily cross-link the polymer with ncSi-$C_x$ coating (see figs. S3 and S4) (*29*–*31*). Furthermore, upon heating, the PESPU polymer molecules and the alkyl ligands tend to vibrate more violently, increasing the probability of cross-linking with each other.

The chemical composition of the three coatings was evaluated through elemental analysis using x-ray photoelectron spectroscopy (XPS). The elemental compositions from low-resolution spectra for all three coatings are listed in table S5. Because of longer alkyl ligands, ncSi-$C_{18}$ has expressed a large amount of carbon content (81.4%) relative to its counterparts, ncSi-$C_{14}$ (76.3%) and ncSi-$C_{10}$ (67.2%). The Si2p content for ncSi-$C_{18}$ was the lowest (3.5%) compared to ncSi-$C_{14}$ (10.1%) and ncSi-$C_{10}$ (13.2%), which could be due to smaller aggregate size of the former. The O1s content is slightly lower for ncSi-$C_{18}$ (11.4%) relative to ncSi-$C_{14}$ (12.1%) and ncSi-$C_{10}$

(16.2%). The lower O1s content could be due to larger $C_{18}$ ligands creating a thicker organic film around the ncSi core, offering higher protection against oxidation (*26*–*28*). In summary, among the three coatings, ncSi-$C_{18}$ has produced a larger number of organic groups and better oxidative stability.

The colloidal size of ncSi-$C_{10}$, ncSi-$C_{14}$, and ncSi-$C_{18}$, measured using dynamic light scattering, was in the range of 342 to 712, 396 to 615, and 190 to 255 nm, respectively (Fig. 5A). The longer alkyl ligand length could increase the distance between particles and overcome van der Waals (VDW) attraction interactions and reduce particle aggregation (*27*, *28*). The uniformity of the nanocoating deposition on the PESPU surface was observed under the scanning electron microscope. Because of smaller aggregates, relative to ncSi-$C_{10}$ and ncSi-$C_{14}$, ncSi-$C_{18}$ produced a more uniform deposition (Fig. 5B). Confocal fluorescence micrographs showed that the pore surfaces were uniformly coated throughout the depth of the ncSi-$C_{18}$ sponge (Fig. 5C). The preliminary adsorption data showed that the ncSi-$C_{18}$–coated sponge exhibited faster crude oil droplets removal (fig. S5). Because of the proximity of carbon ligand length to that of paraffin wax groups (overlaid mass spectra discussed in SEnS-P surface chemistry section) and uniformity of coating, the ncSi-$C_{18}$–based PESPU (i.e., SEnS-P) was selected to evaluate its compatibility with paraffin waxes in the crude oil. Figure 5D shows the coefficient friction calculated as the ratio of the lateral forces to the normal load as a function of the number of sliding cycles for PESPU and SEnS-P. The measurements were performed according to the ASTM G133 standard. For PESPU, a sudden decrease in the friction coefficient from 0.5 to 0.3 was observed over the initial 100 cycles. The coefficient then gradually decreased to 0.26 at the end of 600 cycles, whereas for SEnS-P the coefficient of friction was decreased gradually from 0.55 to 0.3 over the tested 600 cycles. The absence of a sudden drop in coefficient suggests that the coating has not sheared off. Therefore, the nanocoating is considered as mechanically stable under the tested conditions.

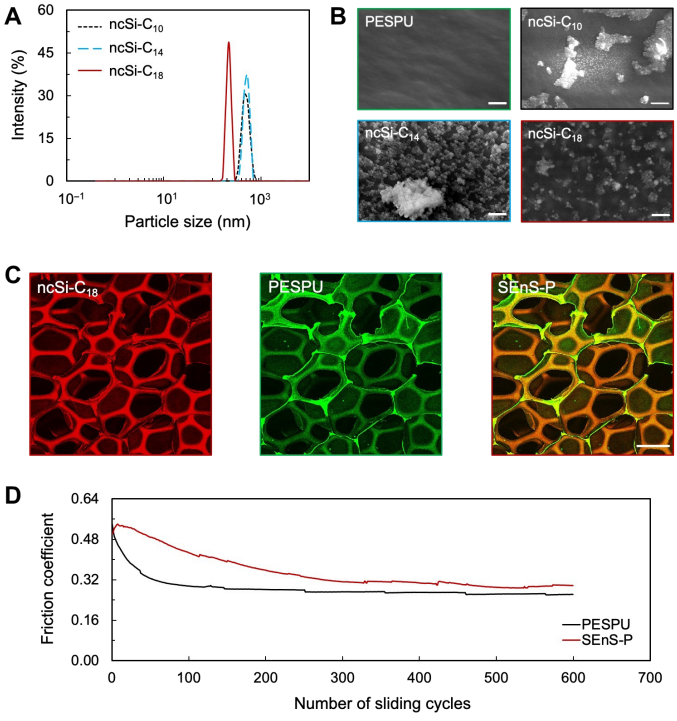


**Fig. 5. Selection of paraffin-like nanocoating.** (**A**) Particle size distribution, obtained using the dynamic light scattering technique, shows the size of the colloidal nanosilicon (ncSi-$C_x$) with increasing ligand length of $x = 10$, 14, and 18 carbons. Among the three coatings, ncSi-$C_{18}$ produced the smallest colloidal size. (**B**) Scanning electron microscopy images show the PESPU substrate before and after applying nanocoatings. Among the three coatings, because of higher stability and smaller colloidal size, ncSi-$C_{18}$ exhibited more uniform deposition on the PESPU surface. (**C**) Confocal image of SEnS-P shows the extent of nanocoating. The nanocoating (red) is uniformly deposited on the open pores of PESPU (green). SEnS-P image (orange) shows ncSi-$C_{18}$ deposited onto the pore surfaces (brown) while flowing through the open cells of the PESPU substrate. However, because of the lack of interaction between the nanosuspension and the closed cells, some of these pores' surfaces contained polymer only (yellow). (**D**) Coefficient of friction versus sliding cycles. The gradual decline in coefficient suggests that the coating is stable. Scale bars, 1 μm (B) and 500 μm (C).

## SEnS-P surface chemistry

The compatibility of the chemical structure between the crude oil and SEnS-P was evaluated using mass spectroscopy. A detailed list of common peaks among the materials is presented in table S6. The overlaid mass spectra show the chemical compatibility of SEnS-P with crude oil (Fig. 6A). The positive-ion spectrum at $m/z$ 0 to 250 shows that, through PESPU and ncSi-$C_{18}$, SEnS-P contains aliphatic surface groups similar to crude oil at $m/z$ 43 ($C_3H_7^+$), 57 ($C_4H_9^+$), and 73 ($C_5H_{13}^+$) and most of the notable peaks between 0 to 250. As can be seen, the ncSi-$C_{18}$ coating has contributed to the higher density of aliphatic groups at the SEnS-P surface. Through PESPU, SEnS-P also contains aromatic groups at $m/z$ 39 ($C_3H_3^+$), 113 ($C_9H_5^+$), and 186 ($C_{15}H_7^+$). The zoomed-in mass spectra at $m/z$ 250 to 500 (Fig. 6B) show that PESPU and ncSi-$C_{18}$ contain heavier organic groups at ion signals $m/z$ 267 ($C_{19}H_{39}^+$), 281 ($C_{20}H_{41}^+$), and 326 ($C_{24}H_{38}^+$). As a result, SEnS-P contains high molecular weight or long hydrocarbons similar to the paraffin groups (long-chain hydrocarbons) in the crude oil. Overall, the mass spectra demonstrate that SEnS-P contains aliphatic, aromatic, and wax groups for adsorbing oil droplets through chemical compatibility.

## Surface energy of SEnS-P

The droplets' wetting at solid surfaces is governed by surface energy. According to the Baier curve, surface energy between 40 and 70 mJ $m^{-2}$ results in good adsorbate adhesion onto solid surfaces, while surface energy between 10 and 20 mJ $m^{-2}$ results in weak adhesion (*32*–*34*). Through ncSi-$C_{18}$ coating, we precisely manipulated the range of surface energies of the PESPU substrate from 110 to 160 mJ $m^{-2}$ (*10*) to 59 to 86 mJ $m^{-2}$. Figure 6C shows the total surface energy ($\gamma_S$) of SEnS-P, which is a summation of the dispersive surface energy ($\gamma_D$) and the acid-base surface energy ($\gamma_{AB}$). $\gamma_D$ maps the energy of Lifshitz-VDW interactions between organic surface groups with *n*-alkane probe molecules. $\gamma_{AB}$ maps the acid-base energy from electrostatic (ES) interactions and hydrogen bond between amphoteric surface groups with polar probe molecules. For SEnS-P, $\gamma_D$ (44 to 64 mJ $m^{-2}$) and $\gamma_{AB}$ (15 to 22 mJ $m^{-2}$) lie in the region of good and weak adhesion, respectively. The thermodynamic work of adhesion between SEnS-P and the crude oil droplets (Fig. 6D) was calculated using Fowke's equation

$$W_{\text{adhesion}} = 2(\gamma_S \gamma_{ow})^{\frac{1}{2}} \quad (4)$$

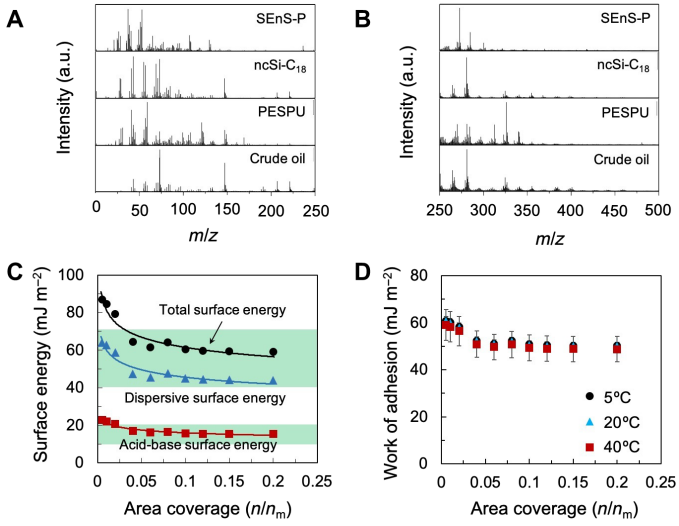


**Fig. 6. Surface properties of SEnS-P.** Overlaid mass spectra of materials at (**A**) *m/z* 0 to 250 and (**B**) *m/z* 250 to 500 show that, through the PESPU substrate and the ncSi-$C_{18}$ coating, SEnS-P achieved a surface chemical structure compatible with the crude oil surface. (**C**) Distribution of surface energy with area coverage. The dispersive and acid-base surface energies of SEnS-P fall within the critical surface energy ranges of 40 to 70 and 10 to 20 mJ $m^{-2}$ required for the adsorption of oil droplets from water. (**D**) Work of adhesion between crude oil droplets and SEnS-P remains constant across all temperatures. The data are an average of three measurements.

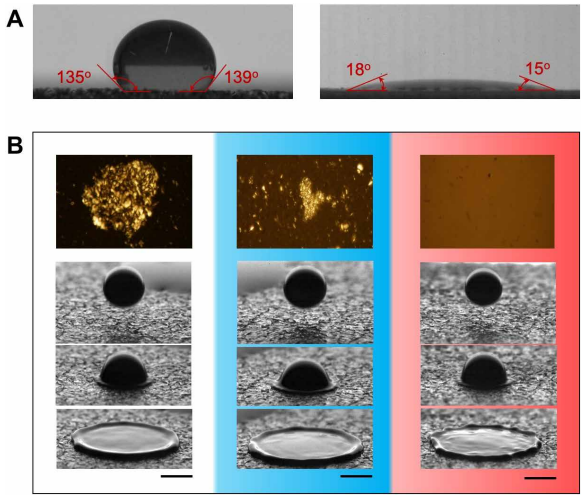


**Fig. 7. Wetting properties of SEnS-P.** (**A**) Wetting of SEnS-P with water (left) and crude oil (right) droplets at room temperature. The water and oil contact angles were measured using the sessile drop method. (**B**) Wettability with temperature with impacting oil droplet. Influence of wax crystalline phase on the crude oil wettability at the SEnS-P surface at 5°C (white), 20°C (blue), and 40°C (red). Scale bars, 1 mm.

and was found to be in the range of 40 to 60 mJ $m^{-2}$. On the basis of the surface energy values, the oil droplets are expected to adhere to SEnS-P by VDW forces, ES forces, and hydrogen bonding. Because of the high density of alkyl groups supplied through the ncSi-$C_{18}$ coating, the $\gamma_D$ value is higher than the $\gamma_{AB}$ value. These results indicate that VDW forces may play a dominant role in droplets adhesion to the SEnS-P surface, which are easier to overcome for oil recovery and SEnS-P reuse.

## Thermoresponsive wetting

SEnS-P exhibited a water contact angle of approximately 139° and an oil contact angle of approximately 15° (Fig. 7A). In flow systems, the wetting properties of solid surfaces are influenced by impact velocity. At approximately 5°, 20°, and 40°C, the wettability of SEnS-P was evaluated with impacting oil droplets at 3 m $s^{-1}$, where droplets wet the surface without splashing (Fig. 7B). At all temperatures, the droplets exhibited excellent wetting at the SEnS-P surface. However, the extent of spreading on SEnS-P varied slightly. At 40°C, because of higher flowability, the oil droplet spread quickly on the film surface. Faster spreading could lead to a slightly higher rate of droplets adsorption.

## Crude oil absorption, emulsions adsorption, and kinetics

Because of hydrophobic ncSi-$C_x$ coating, SEnS-P could exhibit high selectivity for crude oil compared to water. The maximum oil and water uptake capacities of SEnS-P were measured with pure crude oil and pure water separately, and the capacities were calculated gravimetrically (*35*). As shown in fig. S6, because of high selectivity with crude oil, SEnS-P was fully saturated with crude oil within a minute, resulting in 26.77 g of crude oil per gram of SEnS-P. Alternatively, poor water selectivity led to lower water uptake, 1.47 g of water per gram of SEnS-P.

Previously, we reported the influence of emulsified crude oil concentration and pH of the wastewater on the adsorption using sponges (*10*, *11*, *35*, *36*). In current work, the sponges were evaluated for difficult-to-remove dilute emulsions with initial oil concentrations of approximately 10,000 ppm. The oil droplets adsorption onto SEnS-P was experimentally evaluated with freshwater at 5°, 20°, and 40°C, where the wax exists in solid, liquid, and dissolved phases, respectively. SEnS-P removed oil droplets from water at all temperatures with 90 to 99% removal efficacy within 180 min (Fig. 8A). At 5° and 20°C, where the wax is in the solid and liquid crystalline phase, the adsorption was relatively slow, resulting in about 75% oil removal in the initial 30 min, while at 40°C, where all wax is in the dissolved phase, about 97% of the crude oil was adsorbed within the initial 30 min. The slower rate of adsorption is attributed to wax crystallites hindering the flowability of oil droplets at lower temperatures. The maximum oil mass uptake of SEnS-P was in the range of 993 to 1094 mg per gram of SEnS-P across all temperatures (Fig. 8B).

As can be seen, the oil uptake occurred in two stages. The initial oil uptake occurred rapidly, probably due to the physisorption of oil droplets onto the vacant sites at the SEnS-P surface. The subsequent slower oil uptake could be due to fewer vacant sites or a slower pore diffusion. The kinetics of the droplets' adsorption onto SEnS-P was determined using the pseudo–second-order kinetic model (*37*)

$$\frac{t}{Q_{theo}} = \frac{1}{k_2 Q_{exp}^2} + \frac{t}{Q_{exp}} \quad (5)$$

where $Q_{exp}$ is the experimental mass uptake (mg $g^{-1}$), $Q_t$ is the theoretical mass uptake (mg $g^{-1}$), $k_2$ is the adsorption rate constant (mg $g^{-1}$ $min^{-1}$), and $t$ is the time (min). As shown in Fig. 8C, the $t/Q_{exp}$ versus $t$ plot fits linearly at all temperatures. At three temperatures, the kinetic model predicts the oil mass uptakes of 1111 mg $g^{-1}$, which aligns with the experimental oil uptakes of 993 to 1094 mg $g^{-1}$ (see table S7). The small deviation in theoretical and experimental oil mass uptake could be due to experimental error. As expected, the rate of oil adsorption has increased with increasing temperature from 5° to 40°C. Because of wax-wetting properties, SEnS-P could

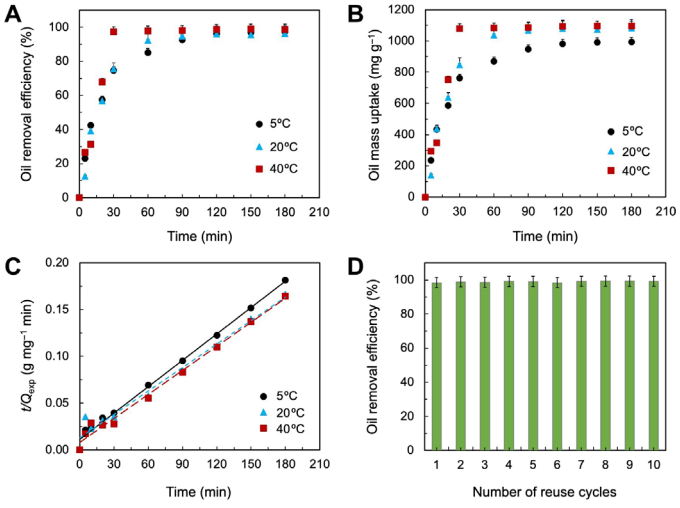


**Fig. 8. Influence of temperature on crude oil droplets adsorption and recovery with SEnS-P.** (**A**) Oil removal efficacy. (**B**) Oil uptake onto SEnS-P. (**C**) Adsorption of crude oil droplets described using a pseudo–second-order kinetic model. (**D**) Reuse of SEnS-P at 40°C. (A to D) The data are the average of at least three trials. These results show that SEnS-P has overcome the crystallization effect of waxes (seen at 5° and 20°C) and achieved high oil droplets removal and recovery from frigid oily wastewater.

adsorb multiphase oil droplets (5° and 20°C), with a similar performance as the pure oil droplets (40°C).

The emulsified crude oil was also removed from synthetic saltwater using SEnS-P to mimic oil extraction processes (fig. S7). SEnS-P was able to adsorb oil droplets from saltwater with 95% removal efficiency within 180 min. Relative to freshwater, SEnS-P has exhibited a slightly higher oil mass uptake of 1182 mg $g^{-1}$ and a higher rate constant of $2.78 \times 10^{-4}$ mg $g^{-1}$ $min^{-1}$ (table S7). The increase in the adsorption kinetics is attributed to enhanced ES attraction interactions between the oil droplets and SEnS-P through $Na^+$ and $Cl^-$ ionic charges (*38*–*40*).

### Adsorbed water, oil recovery, and SEnS-P reuse

Because of critical surface energy, the surface of SEnS-P has preferential adsorption for crude oil droplets, while the water drains through the pores (*11*). Therefore, at the end of the adsorption cycle, the water trapped inside the pore volume of SEnS-P was easy to collect by draining and gentle squeezing. The collected water volume was approximately 3 ml compared to 100 ml of treated water. The adhesion of the oil droplets to the SEnS-P surface was governed predominantly by VDW interactions. Previous work has demonstrated adsorbed oil recovery from SEnS using a linear hydrocarbon solvent—pentane (*11*). In this work, we hypothesized that the oil droplets could adhere to SEnS-P through heavier aromatic-aliphatic compounds, such as wax, resins, and asphaltenes. Therefore, a mixture of aliphatic-aromatic solvents was used to displace the adhered crude oil from SEnS-P. Because of high miscibility, low toxicity, and low cost, heptol was selected as the oil extraction solvent. The heptol ratio of 60% heptane and 40% toluene was selected on the basis of the crude oil's approximate aliphatic and aromatic composition. Because of high miscibility with heptol, the adsorbed oil from SEnS-P was spontaneously recovered within a few seconds (movie S1). In addition, the heptol could act as a diluent in reducing oil viscosity for transporting to refineries. Subsequently, solvents and crude oil can be separated by distillation for further reuse.

The cleaned SEnS-P was reused to adsorb oil droplets from fresh emulsions for 10 cycles at 5° and 40°C. SEnS-P consistently exhibited high oil removal efficiency of 90 to 99%. The reused SEnS-P maintained removal efficacy above 90% with both freshwater and synthetic saltwater at 5°C (fig. S8). This performance is similar to what was observed at 40°C, where the wax crystallites were absent (Fig. 8D). These results suggest that designing sponges by conforming to the thermoresponsive waxes is a practical approach to reclaiming multiphase oil droplets from the frigid water.

## DISCUSSION

Here, by conforming to the thermoresponsive morphology of crude oil droplets, we developed wax-wetting sponges to recover multiphase emulsions and gels from ice-cold water. At low temperatures, crystallized waxes accumulate at the surface of crude oil, increasing its viscosity and hindering flowability. As a result, the collection of heavier droplets from frigid water is an energy-intensive process. Alternatively, because of conformational wax-wetting properties, SEnS-P could recover multiphase oil droplets and gels from cold water via adsorption and solvent extraction processes. We demonstrated this strategy by coating a PESPU sponge with nanosilicon functionalized with paraffin-like groups. ncSi-$C_{18}$ enhances the wax-wetting through paraffin-equivalent surface groups, uniform deposition, and critical surface energy. Adsorption experiments demonstrated that SEnS-P could remove 90 to 99% of oil droplets between 5° and 40°C for 10 cycles. Subsequently, the absorbed crude oil is recovered from the sponge within seconds by displacing it with heptol.

This work advances the efforts underway to cost-effectively recover emulsified crude oil droplets from cold industrial wastewater and oil spills (*41*, *42*). In previous research, photothermal sponges were coupled with in situ joule heating to overcome the viscosity or flowability challenges of the crude oil on a cold marine water surface (*8*, *9*). The innovative wax-wetting sponges eliminate the need for in situ heating, resulting in an energy-efficient, environmentally benign, and easy to implement method. Our results also suggest that mild warming (rather than warming to 90°C) of the immobile oil above pour or cloud point temperatures enhances the flowability of crude oil for removal with sponges. Therefore, we could minimize environmental side effects by reducing the rate of dissolution and evaporation of volatile organic compounds incurred due to excessive heating. Furthermore, spontaneous oil recovery from SEnS-P using heptol, which is a mixture of safer, low-cost solvents, meets environmental standards and improves economic feasibility.

It should be noted that we demonstrated the conformational surface design of sponges using a Texas raw crude, which contains natural paraffin waxes. Other oils will have a different composition and different ratios (saturates, aromatics, resins, and asphaltenes), which would influence the droplets' morphology, rheological properties, and the desired surface properties of sponge. Despite this, the approach could be extended to a wide variety of crude oils that have variable surface properties across a range of environmental conditions, such as oils containing phase-changing waxes, interfacial asphaltenes, and resins or weathered oil. For practical implementation of the sponges, we suggest using our approach of characterizing the influence of environmental conditions (temperature, pH, and salinity) on the physicochemical structure and rheological properties of crude oil and emulsions. Then, the sponge surface properties can be tailored for application over a broad range of environmental

conditions. Similarly, the adsorbed oil extraction solutions need to be tailored for the specific composition of crude oil for enhanced dissolution while adhering to environmental and economic standards. The proposed approach provides insights into designing energy-efficient, low-cost adsorbent sponges to recover difficult-to-remove multiphase emulsions or gels from wastewater. This approach of designing sponges could revolutionize cold water treatment applications for oil sands tailings ponds, marine, and arctic oil spills mitigation.

## MATERIALS AND METHODS

### Preparation of emulsions

The stable oil-in-water emulsions were prepared according to the procedure reported elsewhere (*10*, *11*). Approximately 1 volume % of crude oil was mixed with 100 ml of deionized water in an industrial blender at 22,000 rpm for approximately 30 min. The resulting emulsions had an initial oil concentration of approximately 10,000 mg liter$^{-1}$ and an oil droplet size of ≤10 mm. The emulsions were also prepared with synthetic saltwater by adding 0.1 M NaCl to mimic oil extraction processes.

### Characterization of crude oil and emulsions

#### *Surface chemistry*

Time-of-flight secondary ion mass spectroscopy (TOF-SIMS) is a surface analysis technique that has been used to characterize various materials, including polymers, coatings, and bitumen surfaces (*43*–*45*). We have applied this technique to determine the detailed chemical structure in the outermost molecular layers of the paraffin crude oil surface (Texas raw crude). The silicon wafer substrate used for the oil sample was cleaned in ultraviolet/ozone. Then, a small amount of crude oil was deposited on the silicon wafer using a glass pipette. To avoid molecular migration of the crude oil in the vacuum, the samples were cooled to −80°C. Then, surface analysis was performed immediately using ION-TOF GmbH, Germany. The mass spectra were obtained by probing approximately 100 nm of the outer surface in the static mode. The spectra were acquired in a static mode and by compensating the charge with low-energy electron flooding. An area of approximately 500 μm by 500 μm was analyzed from the probed area to determine the chemical structure. SIMS image analysis was performed using Surface Lab v5 (ION-TOF GmbH). Spatial spectra of crude oil samples were obtained at 10° and 30°C to observe chemical phase segregation with melting.

#### *Thermal analysis*

The crude oil's cloud point and pour point temperatures were determined using differential scanning calorimetry (DSC; Mettler thermoanalytical system TA-3000). The wax content was also verified from the cloud and pour point temperatures using DSC. Before DSC experiments, the samples were precooled to −10°C to ensure complete solidification of the waxes. Approximately 10 mg of crude oil in an aluminum crucible was heated using liquid nitrogen at a rate of 10°C min$^{-1}$ from −10° to 100°C to generate the thermograms. The endothermic (down) peaks represent the phase change of waxes in the crude oil, which were selected as the pour point and cloud point temperatures.

#### *Rheological behavior*

The crude oil rheology experiments were performed with an Anton Paar Rheometer MCR 302 equipped with a Peltier plate and a serrated plate (40 mm diameter). The gap between the parallel plates was approximately 0.6 mm. This gap was selected to minimize the shrinkage effect and to control temperature (*46*). The crude oil samples' desired temperatures were achieved by cooling the sample at a rate of 2°C min$^{-1}$. The oil/water interfacial tension was measured using a spinning drop tensiometer manufactured by KRÜSS GmbH. A borosilicate glass tube was filled with deionized water preequilibrated to pH 5.6. For the selected crude oil and sponge system, this pH provides the best wetting properties by pH-induced charge attraction (*10*). The oil droplet was introduced into the glass tube using a syringe and then spun at 10,000 rpm for 45 min. The desired temperature of the sample was adjusted using an external cooling/heating circulation system. Once the oil droplets' length was approximately four times its width (equilibrium state), the oil/water interfacial tension was calculated using the Vonnegut equation (*20*).

#### *Emulsions' phase behavior with temperature*

The phase behavior of the waxes in the crude oil and emulsions was observed at 5°, 20°, and 40°C. Three different microscope techniques were used to image crude oil or emulsions: optical transmitted light to observe the stability of emulsions, transmitted light with cross-polarized lenses to identify wax crystallites, and fluorescence microscopy to distinguish oil and water phases (*47*). The images were photographed using a cross-polarized microscope (Olympus BX-51) at ×50 magnification and an Olympus C-7070 wide-zoom digital camera at ×4 magnification. Transmitted light with cross-polarized lenses was used to identify wax crystals in the crude oil. Karl-Fischer titration (KAM PKF Portable Karl-Fischer Moisture Analyzer) analysis showed no water content in the pure crude oil. Because of natural fluorescence of the crude oil, fluorescence microscopy is typically used to differentiate petroleum compounds in the water (*47*, *48*). The crude oil (green) and water (black) phases of the emulsified crude oil droplets were differentiated using a confocal fluorescence microscope (ZEISS LSM 880 Elyra Superresolution Imaging System). The selected crude oil has natural fluorescence at wavelengths between 400 and 600 nm. Therefore, images were taken by exciting the samples with the 488-nm laser, while the crude oil was detected at 510 nm. Because of high mechanical mixing speeds, the prepared emulsions exhibited temperatures above 50°C. To evaluate the influence of wax crystallization, the emulsions were cooled to desired temperatures using an ice bath. Upon reaching equilibrium, the oil droplets were observed under the cross-polarized and confocal fluorescence light microscopes.

### Fabrication and characterization of adsorbents

#### *Synthesis of nanocoatings*

A detailed list of regents, materials, and protocol for the nanocoating synthesis can be found in section S2. The nanocoatings were synthesized by functionalizing the nanosilicon capped with decyl, tetradecyl, and octadecyl using the thermal hydrosilylation reaction (*49*). The reaction with 1-decene was carried out at 170°C for 1.5 hours, whereas, due to the higher boiling temperatures of 1-tetradecyl and 1-octadecene, the hydrosilylation with them was performed at 190°C. The high reaction temperatures are required for increasing the density of alkyl ligands capping on the ncSi surface and to reduce particle-particle attraction (*27*, *28*). The aggregation of functionalized nanocoatings was observed under a transmission electron microscope (Talos L120C). The colloidal size of nanomaterials was determined by dynamic light scattering (Zetasizer Nano ZS, Malvern Instruments).

### *Fabrication of SEnS-P*

A detailed protocol on the dip coating process is presented in section S2. SEnS-P was fabricated by coating approximately 0.6 weight % of ncSi-$C_{10}$, ncSi-$C_{14}$, and ncSi-$C_{18}$ on the porous PESPU substrate via the dip-and-dry method followed by annealing in air at 170°C. Previously, we determined this weight % as the required nanocoating dosage to achieve the critical surface energy at the PESPU surface (*11*). The post-annealing initiates ncSi-$C_{18}$ cross-linking with the PESPU sponge through oxidative initiation via heat (*29*–*31*). The nanocoating distribution on the PESPU surface was observed using scanning electron microscope (JEM-2010, JEOL). The deposition of the nanocoating on the inside of the pore surfaces was observed using a confocal microscope (Nikon A1). For contact angle measurements, SEnS-P films were fabricated by pressing using a compression mold.

### *Surface chemistry*

The surface chemical structure of ncSi-$C_{18}$, PESPU, and SEnS-P was characterized using TOF-SIMS. The ncSi-$C_{18}$ suspensions were deposited on the silicon wafer using a glass pipette. For all the materials, the mass spectra were obtained at room temperature in the static mode of the instrument. The ion signals were analyzed using Surface Lab v5 (ION-TOF GmbH). Refer to (*43*) for methodology used to characterize the polymers and nanosilicon. Change in elemental composition at the nanocoated sponge surfaces was characterized using XPS (Thermo Fisher Scientific, E. Grinstead, UK). XPS was equipped with monochromatic Al Kα x-ray radiation and a hemispherical electron energy analyzer. The XPS data were processed using Avantage v.5.926 software. FTIR spectroscopy was performed on a Perkin-Elmer Spectrum One FTIR spectrometer with the attenuated total reflection mode, which enabled direct acquisition of the spectra of solid samples.

### *Surface energy*

For surface energy measurements, approximately 10 mg of SEnS-P sample was packed into a salinized glass column (300 mm in length and 4 mm in diameter). The surface energy of SEnS-P was measured using inverse gas chromatography (IGC) manufactured by Surface Measurement Systems, Appleton, UK (model IGC-SEA), and the data were analyzed using SEA Analysis software. Before measurements, the samples were preconditioned to 30°C for 120 min using helium. Methane was used for dead volume correction. The dispersive surface energy was measured using *n*-alkane probe molecules, heptane, octane, nonane, and decane and described using the Dorris and Gray method (*50*). The acid-base surface energy was measured with polar probe molecules—acetone, methanol, ethyl acetate, and dichloromethane—and described using the van Oss–Good–Chaudhury model (*51*).

### *Coefficient of friction*

A nano tribometer was used to characterize the coefficient of friction of the underwater PESPU and SEnS-P. A 2-mm-diameter $Al_2O_3$ ball with a smooth surface was mounted in a carrier head and oscillated against a stationary planar specimen with an applied load of 75 mN. The sliding speed was approximately 18.85 mm $s^{-1}$, and the stroke length was approximately 3 mm. Before testing, the sponges were immersed in water to mimic underwater operation. The test was carried out at ambient conditions. The coefficient of friction was measured for each sample independently. The values at the middle of each cycle was considered as the cycle-averaged value.

### *Contact angles*

For contact angle measurements, the water and oil droplets were placed on SEnS-P films using a flat-tipped hypodermic needle (Hamilton, N733 at 0.5"PT3). The wetting of impacting droplets on SEnS-P films was measured at 500 frames per second (fps) using a high-speed imaging camera (Photron FASTCAM SA5). All the images were processed using Fiji software (version 2.0.0) (*52*).

## Oil droplets absorption, adsorption, and recovery processes

### *Absorption experiments*

The crude oil and water absorption experiments were performed via gravimetric analysis (*35*). Approximately, 2 cm by 2 cm by 2 cm of SEnS-P samples were placed on the crude oil or water surface. At preselected intervals, the samples were removed, and the weights were recorded. The change is that sample weights were used to estimate the maximum crude oil and water absorption capacity according to

$$\text{Uptake capacity} = \frac{(m_t - m_o)}{m_o} \quad (6)$$

where $m_t$ is the instantaneous mass of the sponge in grams, and $m_o$ is the initial mass of the sponge in grams.

### *Adsorption experiments*

SEnS-P adsorption experiments were conducted with oil/water emulsions at pH 5.6 and at 5°, 20°, and 40°C. In these experiments, a SEnS-P sample of approximately 0.85 g was submerged in approximately 100 ml of emulsion. The preparation and characterization of emulsions are reported elsewhere (*10*, *11*). At the desired temperature, SEnS-P was held stationary in the emulsions, which were stirred at 500 rpm for 3 hours. The emulsions were cooled to 5° and 20°C using a Peltier cooling system. A hot plate was used to preheat the emulsions to 40°C. The temperature of the emulsions was monitored using a thermocouple. Water samples (1 ml) were collected at predetermined time intervals and analyzed for oil concentration using a total organic carbon analyzer (Shimadzu, TOC-VCPN). The difference in oil concentration levels was used to estimate the emulsified oil removal efficiency and adsorption. The oil removal efficacy was calculated as

$$\eta\,\% = \frac{(C_o - C_t)}{C_o} \times 100 \quad (7)$$

where η% is the oil removal efficacy in percentage and $C_o$ and $C_t$ represent the oil concentration in the water in mg $liter^{-1}$ at the beginning and at the selected time step, respectively. The adsorption capacity of SEnS-P was calculated according to

$$Q_{exp} = \frac{(C_o - C_t)\,V}{m} \quad (8)$$

where, $Q_{exp}$ is the experimental oil uptake of SEnS-P in mg $g^{-1}$, $V$ is the total volume of the emulsions in liters, and $m$ is the initial weight of SEnS-P in grams. To select the best nanocoating, sponges coated with different carbon chain lengths were assessed by monitoring turbidity change during adsorption experiments (*36*). The turbidity analysis of water samples was performed using a LaMotte (LTC-3000we) turbidity meter.

### *SEnS-P regeneration*

The crude oil adsorbed SEnS-P was regenerated using mechanical compression and solvent wash based on the previously reported protocols (*11*). After each adsorption cycle, SEnS-P was slightly compressed to remove trapped water from the pores. Because of enhanced adhesion of the liquid and wax crystallites, SEnS-P regeneration with pentane alone was not effective. Furthermore, according to the Pfizer green solvents list, pentane has toxicity concerns

(*53*, *54*). Therefore, the adhered crude oil from SEnS-P was collected by displacing it with a mixture of safe to use solvents, heptane, and toluene at a ratio of 60 and 40%, respectively. SEnS-P was first compressed to drain the residual solvent, then dried at 80°C in a vacuum furnace for 30 min, and reused to remove oil droplets from fresh emulsion samples.

## SUPPLEMENTARY MATERIALS

Supplementary material for this article is available at http://advances.sciencemag.org/cgi/content/full/7/11/eabc7926/DC1

## REFERENCES AND NOTES


1. Alberta Environment and Parks, Mineable oil sands fluid tailings volume by facility as of the end of 2013. Oil Sands Information Portal, Alberta Environment and Parks, Edmonton, AB. Dataset no. 540. http://osip.alberta.ca/library/Dataset/Details/540 [accessed 2 September 2020].
2. G. Whiteman, C. Hope, P. Wadhams, Climate science: Vast costs of arctic change. *Nature* **499**, 401–403 (2013).
3. J. P. Incardona, L. D. Gardner, T. L. Linbo, T. L. Brown, A. J. Esbaugh, E. M. Mager, J. D. Stieglitz, B. L. French, J. S. Labenia, C. A. Laetz, M. Tagal, C. A. Sloan, A. Elizur, D. D. Benetti, M. Grosell, B. A. Block, N. L. Scholz, PNAS Plus: From the Cover: Deepwater horizon crude oil impacts the developing hearts of large predatory pelagic fish. *Proc. Natl. Acad. Sci. USA* **111**, E1510–E1518 (2014).
4. G. Kwon, A. K. Kota, Y. Li, A. Sohani, J. M. Mabry, A. Tuteja, On-demand separation of oil-water mixtures. *Adv. Mater.* **24**, 3666–3671 (2012).
5. E. Barry, J. A. Libera, A. U. Mane, J. R. Avila, D. DeVitis, K. Van Dyke, J. W. Elam, S. B. Darling, Mitigating oil spills in the water column. *Environ. Sci. Water Res. Technol.* **4**, 40–47 (2018).
6. E. Barry, A. U. Mane, J. A. Libera, J. W. Elam, S. B. Darling, Advanced oil sorbents using sequential infiltration synthesis. *J. Mater. Chem. A* **5**, 2929–2935 (2017).
7. H. Y. Mi, X. Jing, H. X. Huang, L. S. Turng, Controlling superwettability by microstructure and surface energy manipulation on three-dimensional substrates for versatile gravity-driven oil/water separation. *ACS Appl. Mater. Interfaces* **9**, 37529–37535 (2017).
8. J. Ge, L. A. Shi, Y. C. Wang, H. Y. Zhao, H. B. Yao, Y. B. Zhu, Y. Zhang, H. W. Zhu, H. A. Wu, S. H. Yu, Joule-heated graphene-wrapped sponge enables fast clean-up of viscous crude-oil spill. *Nat. Nanotechnol.* **12**, 434–440 (2017).
9. M. Wu, Y. Shi, J. Chang, R. Li, C. Ong, P. Wang, Sunlight induced rapid oil absorption and passive room-temperature release: An effective solution toward heavy oil spill cleanup. *Adv. Mater. Interfaces* **5**, 1800412 (2018).
10. P. Cherukupally, E. J. Acosta, J. P. Hinestroza, A. M. Bilton, C. B. Park, Acid–base polymeric foams for the adsorption of micro-oil droplets from industrial effluents. *Environ. Sci. Technol.* **51**, 8552–8560 (2017).
11. P. Cherukupally, W. Sun, A. P. Y. Wong, D. R. Williams, G. A. Ozin, A. M. Bilton, C. B. Park, Surface-engineered sponges for recovery of crude oil microdroplets from wastewater. *Nat. Sustain.* **3**, 136–143 (2020).
12. S. W. Ferris, H. C. Cowles, Crystal behavior of paraffin wax. *Ind. Eng. Chem.* **37**, 1054–1062 (1945).
13. J. Giermanska, F. Thivilliers, R. Backov, V. Schmitt, N. Drelon, F. Leal-Calderon, Gelling of oil-in-water emulsions comprising crystallized droplets. *Langmuir* **23**, 4792–4799 (2007).
14. F. Thivilliers, E. Laurichesse, H. Saadaoui, F. Leal-Calderon, V. Schmitt, Thermally induced gelling of oil-in-water emulsions comprising partially crystallized droplets: The impact of interfacial crystals. *Langmuir* **24**, 13364–13375 (2008).
15. A. Japper-Jaafar, P. T. Bhaskoro, Z. S. Mior, A new perspective on the measurements of wax appearance temperature: Comparison between DSC, thermomicroscopy and rheometry and the cooling rate effects. *J. Pet. Sci. Eng.* **147**, 672–681 (2016).
16. E. Andrade, The viscosity of liquids. *Nature* **125**, 309–310 (1930).
17. E. Andrade, Viscosity of liquids. *Proc. R. Soc. A* **215**, 36–43 (1952).
18. M. Geri, R. Venkatesan, K. Sambath, G. H. McKinley, Thermokinematic memory and the thixotropic elasto-viscoplasticity of waxy crude oils. *J. Rheol.* **61**, 427–454 (2017).
19. C. Giavarini, F. Pochetti, Characterization of petroleum products by DSC analysis. *J. Therm. Anal. Calorim.* **5**, 83–94 (1973).
20. B. Vonnegut, Rotating bubble method for the determination of surface and interfacial tensions. *Rev. Sci. Instrum.* **13**, 6–9 (1942).
21. D. L. Dorset, Crystallography of real waxes: Branched chain packing in microcrystalline petroleum wax studied by electron diffraction. *Energy Fuel* **14**, 685–691 (2000).
22. R. Varadaraj, C. Bron, Molecular origins of heavy crude oil interfacial activity part 2: Fundamental interfacial properties of model naphthenic acids and naphthenic acids separated from heavy crude oils. *Energy Fuel* **21**, 199–204 (2007).
23. A. M. Atta, H. I. Al-Shafy, E. A. Ismail, Influence of ethylene acrylic alkyl ester copolymer wax dispersants on the rhological behavior of Egyptian crude oil. *J. Dispers. Sci. Technol.* **32**, 1296–1305 (2011).
24. X. Zhao, P. Liu, L. Ye, Synthesis, structure and phase transition property of acrylic acid grafted paraffin. *J. Mol. Struct.* **1064**, 37–43 (2014).
25. Y. Zhang, R. Mandal, D. C. Ratchford, R. Anthony, J. Yeom, Si nanocrystals/ZnO nanowires hybrid structures as immobilized photocatalysts for photodegradation. *Nanomaterials* **10**, 491 (2020).
26. Z. Yang, M. Iqbal, A. R. Dobbie, J. G. Veinot, Surface-induced alkene oligomerization: Does thermal hydrosilylation really lead to monolayer protected silicon nanocrystals? *J. Am. Chem. Soc.* **135**, 17595–17601 (2013).
27. M. G. Panthani, C. M. Hessel, D. Reid, G. Casillas, M. José-Yacamán, B. A. Korgel, Graphene-supported high-resolution TEM and STEM imaging of silicon nanocrystals and their capping ligands. *J. Phys. Chem. C* **116**, 22463–22468 (2012).
28. B. L. V. Prasad, S. I. Stoeva, C. M. Sorensen, K. J. Klabunde, Digestive ripening of thiolated gold nanoparticles: The effect of alkyl chain length. *Langmuir* **18**, 7515–7520 (2002).
29. E. Yousif, R. Haddad, Photodegradation and photostabilization of polymers, especially polystyrene: Review. *Springerplus* **2**, 398 (2013).
30. J. F. Rabek, *Polymer Degradation Mechanisms and Experimental Methods* (Stocholm, 1994), p. 50.
31. J. F. Rabek, *Polymer Degradation Mechanisms and Experimental Methods* (Stocholm, 1994), p. 62.
32. R. E. Baier, E. G. Shafrin, W. A. Zisman, Adhesion: Mechanisms that assist or impede it. *Science* **162**, 1360–1368 (1968).
33. R. E. Baier, The role of surface energy in thrombogenesis. *Bull. N. Y. Acad. Med.* **48**, 257–272 (1972).
34. R. E. Baier, J. G. Michalovic, V. A. Depalma, R. J. Pilie, Universal gelling agent for the control of hazardous liquid spills. *J. Hazard. Mater.* **1**, 21–33 (1975).
35. P. Cherukupally, R. K. M. Chu, A. M. Bilton, C. B. Park, Oil diffusion properties of acoustic foams for oil contaminated water treatment. *AIP Conf. Proc.* **1779**, 050011 (2016).
36. P. Cherukupally, J. H. Hinestroza, R. Farnood, A. M. Bilton, C. B. Park, Adsorption mechanisms of emulsified crude oil droplets onto hydrophilic open-cell polymer foams. *AIP Conf. Proc.* **1914**, 170003 (2017).
37. Y. S. Ho, G. McKay, Pseudo-second order model for sorption processes. *Process Biochem.* **34**, 451–465 (1999).
38. M. Kullappan, M. K. Chaudhury, Extraction of organic-free water from detergent stabilized emulsion. *Ind. Eng. Chem. Res.* **58**, 21089–21104 (2019).
39. L. S. McCarty, G. M. Whitesides, Electrostatic charging due to separation of ions at interfaces: Contact electrification of ionic electrets. *Angew. Chem. Int. Ed.* **47**, 2188–2207 (2008).
40. F. Mugele, B. Bera, A. Cavalli, I. Siretanu, A. Maestro, M. Duits, M. Cohen-Stuart, D. van den Ende, I. Stocker, I. Collins, Ion adsorption-induced wetting transition in oil-water-mineral systems. *Sci. Rep.* **5**, 10519 (2015).
41. A. Abidli, Y. Huang, P. Cherukupally, A. M. Bilton, C. B. Park, Novel separator skimmer for oil spill cleanup and oily wastewater treatment: From conceptual system design to the first pilot-scale prototype development. *Environ. Technol. Innov.* **18**, 100598 (2020).
42. P. Cherukupally, A. M. Bilton, J. Hinestroza, C. B. Park, "Micro organic pollutants removal using a foam filter through rationally selected hydrophilic media" (SPE-ANTEC Technical Paper, 2017).
43. X. Lu, P. Sjövall, H. Soenen, Structural and chemical analysis of bitumen using time-of-flight secondary ion mass spectrometry (TOF-SIMS). *Fuel* **199**, 206–218 (2017).
44. A. Iuraş, D. J. Scurr, C. Boissier, M. L. Nicholas, C. J. Roberts, M. R. Alexander, Imaging of crystalline and amorphous surface regions using time-of-flight secondary-ion mass spectrometry (ToF-SIMS): Application to pharmaceutical materials. *Anal. Chem.* **88**, 3481–3487 (2016).
45. R. N. Sodhi, Time-of-flight secondary ion mass spectrometry (TOF-SIMS): Versatility in chemical and imaging surface analysis. *Analyst* **129**, 483–487 (2004).
46. F. H. Marchesini, A. A. Alicke, P. R. de Souza Mendes, C. M. Ziglio, Rheological characterization of waxy crude oils: Sample preparation. *Energy Fuel* **26**, 2566–2577 (2011).
47. S. K. Kiran, S. Ng, E. J. Acosta, Impact of asphaltenes and naphthenic amphiphiles on the phase behavior of solvent–bitumen–water systems. *Energy Fuel* **25**, 2223–2231 (2011).
48. J. Steffens, E. Landulfo, L. C. Courrol, R. Guardani, Application of fluorescence to the study of crude petroleum. *J. Fluoresc.* **21**, 859–864 (2011).
49. W. Sun, C. Qian, M. L. Mastronardi, M. Wei, G. A. Ozin, Hydrosilylation kinetics of silicon nanocrystals. *Chem. Commun.* **49**, 11361–11363 (2013).
50. P. P. Ylä-Mäihäniemi, J. Y. Y. Heng, F. Thielmann, D. R. Williams, Inverse gas chromatographic method for measuring the dispersive surface energy distribution for particulates. *Langmuir* **4**, 9551–9557 (2008).
51. C. J. Van Oss, R. J. Good, M. K. Chaudhury, Additive and nonadditive surface tension components and the interpretation of contact angles. *Langmuir* **4**, 884–891 (1988).
52. J. Esmaeelpanah, P. Cherukupally, S. Chandra, J. Mostaghimi, Numerical and experimental investigation of bubble attachment to a substrate, *Proc. TFESC Conf.* (2015); https://doi.org/10.1615/TFESC1.mph.012563.

53. K. Alfonsi, J. Colberg, P. J. Dunn, T. Fevig, S. Jennings, T. A. Johnson, H. P. Kleine, C. Knight, M. A. Nagy, D. A. Perry, M. Stefaniak, Green chemistry tools to influence a medicinal chemistry and research chemistry based organisation. *Green Chem.* **10**, 31–36 (2008).
54. D. Prat, J. Hayler, A. Wells, A survey of solvent selection guides. *Green Chem.* **16**, 4546–4551 (2014).

**Acknowledgments:** We thank K. Volchek at Environment and Climate Change Canada for informative discussions on the challenges associated with oil spill cleanup. We acknowledge J. McGroarty for assistance with the material fabrication and adsorption experiments. We thank E. Acosta at the University of Toronto for providing access to the polarized microscope and TOC analyzer. Also, we appreciate M. Trusler and P. Cary at Imperial College London for their guidance and providing access to laboratory resources in crude oil characterization. We also thank R. Sodhi for mass spectroscopy, J. Bouchard for high-speed contact angles, and A. Kondor for surface energy measurements. We appreciate helpful discussions on the emulsions crystallization with C. Holtze at BASF. **Funding:** We appreciate the financial support of the Department of Fisheries and Oceans Canada (MECTS-3955465), Canada Foundation for Innovation (CFI, 32974), Natural Sciences and Engineering Research Council of Canada Discovery Grant, Research England Global Challenges Research Fund, UK Research and Innovation, and National Natural Science Foundation of China (grant no. 51902287). **Author contributions:** P.C. designed the research and adsorption-recovery process; performed literature review, materials characterization, oil adsorptive-recovery experiments, and modeling; analyzed data; curated figures; and wrote the manuscript. W.S. developed and performed materials fabrication and literature review, analyzed results, and reviewed the manuscript. D.R.W., G.A.O., and A.M.B. advised with surface science, nanoscience, and water treatment aspects of the work, respectively. A.M.B. edited the manuscript. All authors critically reviewed and approved the manuscript. A.M.B. is the principal investigator of the project. **Competing interests:** The authors declare that they have no competing interest. **Data and materials availability:** All data needed to evaluate the conclusions in the paper are present in the paper and/or the Supplementary Materials. Additional data related to this paper may be requested from P.C.

Submitted 14 May 2020
Accepted 26 January 2021
Published 10 March 2021
10.1126/sciadv.abc7926

**Citation:** P. Cherukupally, W. Sun, D. R. Williams, G. A. Ozin, A. M. Bilton, Wax-wetting sponges for oil droplets recovery from frigid waters. *Sci. Adv.* **7**, eabc7926 (2021).

# Wax-wetting sponges for oil droplets recovery from frigid waters

P. Cherukupally, W. Sun, D. R. Williams, G. A. Ozin and A. M. Bilton

*Sci Adv* **7** (11), eabc7926.
DOI: 10.1126/sciadv.abc7926